Aerial Reconfigurable Intelligent Surface-Assisted Channel Modeling Incorporating the Effect of UAV Fluctuations

Zili Wang, Ji Bian, *Member, IEEE*, Cheng-Xiang Wang, *Fellow, IEEE*, Yu Liu, *Member, IEEE*, and Jie Tian, *Member, IEEE*

***Abstract*— Aerial reconfigurable intelligent surface (ARIS) system refers to a novel transmission scheme, in which an RIS is mounted on aerial platforms, such as unmanned aerial vehicles (UAVs), to achieve intelligent signal reflection over the air. Compared to terrestrial RIS, ARIS extends the service area and enables panoramic signal reflections. Benefiting from its high altitude, the UAV is more likely to establish line-of-sight (LoS) connections with ground nodes. However, implementing ARIS systems is challenging. Owing to atmospheric turbulence or propeller rotations, the UAV can experience random fluctuations, which lead to misalignment of reflected signal phases. In this letter, a three-dimensional (3D) ARIS-assisted channel model is proposed, in which UAV fluctuations are described by random processes. Statistics including temporal correlation function (TCF), Doppler power spectral density (PSD), and ergodic achievable rate are obtained. Results show that even for a minor vibration, the UAV wobbling can introduce extra Doppler frequency components, and significantly reduce the temporal correlation and achievable rate of the ARIS-assisted channel when systems operating at high frequency bands.**

***Index Terms*— Reconfigurable intelligent surface, unmanned aerial vehicle, UAV fluctuations, channel statistics, channel models.**

I. Introduction

RECONFIGURABLE intelligent surface (RIS) is a planar array composed of numerous reflection units (RUs), which can manipulate phases and/or amplitudes of incoming waves to generate a virtual beam directed toward a specific destination [1]. The programmable capability allows the RIS to control wireless propagation environments. To facilitate the system design and assess communication technologies, it is imperative to construct channel models that can uncover the fundamental channel properties [2], [3]. In [4], a three-dimensional (3D) channel model for RIS-aided air-to-ground (A2G) communications was developed by decomposing the RIS-assisted channel into unmanned aerial vehicle (UAV)-RIS and RIS-receiver (Rx) subchannels, where the latter was described by the ellipsoid model. A cluster-based RIS-aided A2G model was presented in [5], in which the RIS was modeled as a special single-bounce cluster with adjustable phases. In typical vehicle-to-vehicle scenarios, the transmitter (Tx) and Rx antennas are usually mounted at relatively low heights and surrounded by numerous obstacles. The paths between the Tx/Rx and terrestrial RIS can easily become obstructed. To overcome this limitation, a practical solution is to deploy the RIS on aircraft, such as UAVs, which is called aerial reconfigurable intelligent surface (ARIS) [6], [7]. Thanks to the high maneuverability of UAVs, they can navigate to avoid obstacles and establish reliable line-of-sight (LoS) connections with ground nodes. Additionally, ARIS can effectively utilize the entire 3D space, in contrast to terrestrial RIS, where the Tx and Rx are located on the same side of the RIS. In [8], an ARIS channel model was presented using a single cylinder model. The results showed that the multipath fading and Doppler effects were alleviated by using the adjustable reflection phases. In realistic scenarios, the hovering UAV may experience random fluctuations due to atmospheric turbulence. In [9], an A2G model was introduced, focusing on the pitch angle of UAV rotation. In contrast, the A2G model in [10] captured UAV vibration by modeling the periodic changes in the UAV's radial velocity. As far as we know, none of the existing ARIS channel models takes the UAV fluctuations into consideration, and the impacts of UAV fluctuations on the ARIS channel behaviors are still unknown.

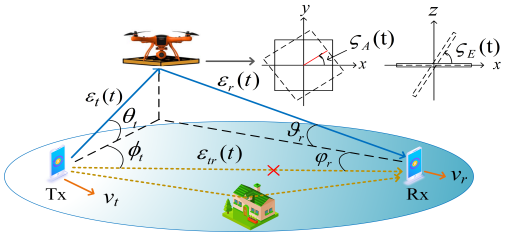

Fig. 1. Geometrical characteristics of the 3D channel model for ARIS-assisted communication scenarios.

This letter presents a 3D ARIS-assisted channel model that considers the large-scale and micro-scale mobilities of the UAV, referring to the UAV flying in specific directions and experiencing random fluctuations. Statistics of the model are derived and the impacts of UAV fluctuations on those statistics are investigated.

Fig. 1 shows a typical ARIS-assisted communication scenario. The initial position of the Tx is selected as the origin of the coordinates, and the initial location of the Rx is defined as $(\varepsilon_{tr}, 0, 0)$. It is assumed that the direct path from Tx to Rx is blocked by obstructions [5]. To enhance the system performance, an RIS comprising K_x columns and K_y rows

Manuscript received 7 March 2024; revised 7 April 2024; accepted 25 April 2024. Date of publication 30 April 2024; date of current version 12 July 2024. This work was supported by the National Natural Science Foundation of China (NSFC) under Grants 62101311, 62271295, and 61960206006, and the Key Technologies R&D Program of Jiangsu (Prospective and Key Technologies for Industry) under Grants BE2022067 and BE2022067-1. The associate editor coordinating the review of this letter and approving it for publication was F. El-Bouanani. *(Corresponding author: Ji Bian.)*

Zili Wang, Ji Bian, and Jie Tian are with the School of Information Science and Engineering, Shandong Normal University, Jinan 250358, China (e-mail: wzili22@163.com; jibian@sdnu.edu.cn; tianjie@sdnu.edu.cn).

Cheng-Xiang Wang is with the National Mobile Communications Research Laboratory, School of Information Science and Engineering, Southeast University, Nanjing 210096, China, and also with Purple Mountain Laboratories, Nanjing 211111, China (e-mail: chxwang@seu.edu.cn).

Yu Liu is with the School of Integrated Circuit, Shandong University, Jinan 250101, China (e-mail: yuliu@sdu.edu.cn).

Digital Object Identifier 10.1109/LCOMM.2024.3395489

1558-2558 © 2024 IEEE. Personal use is permitted, but republication/redistribution requires IEEE permission.
See https://www.ieee.org/publications/rights/index.html for more information.

Authorized licensed use limited to: Southeast University. Downloaded on July 12,2024 at 02:10:16 UTC from IEEE Xplore. Restrictions apply.

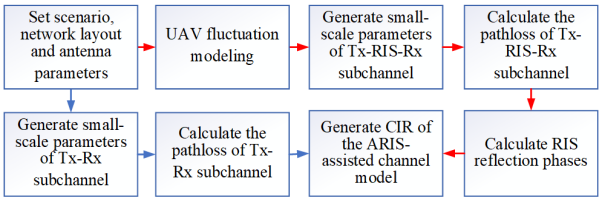

Fig. 2. The procedure of generating the CIR of the proposed model.

of passive RUs is mounted on a UAV, whose initial position is (x_u, y_u, H_u). The spacings between adjacent columns and rows of the RUs are denoted by δ_x and δ_y, respectively. In addition, the UAV moves with a speed of v_u and travels with an azimuth angle α_u. Both the Tx and Rx are equipped with single omnidirectional antennas. The Tx is moving with the speed v_t and travel azimuth angle α_t, whereas the Rx is moving with the speed v_r and travel azimuth angle α_r.

For convenience, we assume that the UAV and the RIS share the same center. Thus, the initial distance between Tx and RIS center is $\varepsilon_t = \sqrt{x_u^2 + y_u^2 + H_u^2}$, and the initial distance from RIS center to the Rx is $\varepsilon_r = \sqrt{(x_u - \varepsilon_{tr})^2 + y_u^2 + H_u^2}$. In addition, ϕ_t and θ_t are the azimuth and elevation angles of departure of the waves impinging on the RIS, respectively, and are calculated as $\phi_t = \text{atan2}(y_u, x_u)$ and $\theta_t = \arctan\left(\frac{H_u}{\sqrt{x_u^2+y_u^2}}\right)$, where atan2$(\cdot)$ is the four-quadrant inverse tangent function. Similarly, $\varphi_r = \text{atan2}(y_u, x_u - \varepsilon_{tr})$ and $\vartheta_r = \arctan\left(\frac{H_u}{\sqrt{(x_u-\varepsilon_{tr})^2+y_u^2}}\right)$ are the azimuth and elevation angles of arrival of waves reflected by RIS, respectively. The procedure of generating the channel impulse response (CIR) of the proposed model is shown in Fig. 2.

II. ARIS-Assisted Channel Model

A. UAV Fluctuation Modeling

As shown in Fig. 1, the wobbling angles in horizontal and vertical planes are measured by the yaw angle $\zeta_A(t)$ and pitch angle $\zeta_E(t)$, respectively, which are modeled as

$$\zeta_A(t) = \zeta_A(t_0) + \xi_A \cdot \sin(2\pi f_w t) \quad (1)$$

$$\zeta_E(t) = \zeta_E(t_0) + \xi_E \cdot \sin(2\pi f_w t) \quad (2)$$

where $t_0 = 0$ indicates the initial time instant, $\xi_{A(E)}$ and f_w are independent random variables describing the amplitudes and frequencies of wobbling angles, respectively, which follow specific distributions [9].

B. Small-Scale Fading

The CIR of the ARIS-aided channel can be expressed as

$$h(t,\tau) = \sqrt{PL_{\text{RIS}}^{-1}} \cdot h_{\text{RIS}}(t,\tau) + \sqrt{PL_{\text{env}}^{-1}} \cdot h_{\text{env}}(t,\tau) \quad (3)$$

where PL_{RIS} and PL_{env} are the pathloss of the Tx–RIS–Rx and Tx–Rx subchannels, respectively. It is assumed that the UAV can avoid obstacles and establish strong LoS paths to the terrestrial nodes. Note that at millimeter wave (mmWave) bands, LoS paths tend to be considerably stronger than non-line-of-sight (NLoS) paths due to the severe pathloss and significant penetration loss [11]. For simplicity, only LoS paths between the UAV and ground nodes were taken into account. The CIR of Tx–RIS–Rx subchannel that captures small-scale fading is modeled as

$$h_{\text{RIS}}(t,\tau) = \sum_{k=1}^{K} J_k e^{j[\psi_k(t)+\chi_{tk}(t)+\chi_{kr}(t)]} \cdot \delta(\tau - \tau_k) \quad (4)$$

where $K = K_x \times K_y$, $J_k = \frac{1}{\sqrt{K}}$ and τ_k are the gain and delay of the ray reflected by the kth RU, i.e., RU$_k$, respectively. Furthermore, ψ_k is the phase shift of RU$_k$, $\chi_{tk}(t) = \frac{2\pi\varepsilon_{tk}(t)}{\lambda}$, $\chi_{kr}(t) = \frac{2\pi\varepsilon_{kr}(t)}{\lambda}$ represents the phase shifts of the wave due to the travel distances. Specifically, $\varepsilon_{tk}(t)$ and $\varepsilon_{kr}(t)$ are time-varying distances of Tx–RU$_k$ and RU$_k$–Rx, respectively, $\lambda = c/f_c$ is the wavelength, f_c is carrier frequency, c is the speed of light. The delay is obtained as $\tau_k = \frac{\varepsilon_{tk}(t)+\varepsilon_{kr}(t)}{c}$.

Proposition 1: The travel distances of Tx–RU$_k$ at time t can be calculated as

$$\varepsilon_{tk}(t) \approx \varepsilon_t(t) + \Delta_k \cdot \cos\theta_t \cdot [\cos(\alpha_k - \phi_t) - \sin(\alpha_k - \phi_t) \cdot \zeta_A(t)] + \Delta_k \cdot \sin\theta_t \cdot \zeta_E(t). \quad (5)$$

Considering the short observation interval, the time-varying distance from Tx to the RIS center is $\varepsilon_t(t) \approx \varepsilon_t + v_u t \cos\theta_t \cos(\phi_t - \alpha_u) - v_t t \cos\theta_t \cos(\phi_t - \alpha_t)$. Furthermore, Δ_k denotes the distance between the RIS center and RU$_k$, and α_k represents the angle between the x-axis and the line connecting the RIS center and RU$_k$ in the xy plane, which are respectively expressed as

$$\Delta_k = \frac{1}{2}\sqrt{[(K_x - 2k_x + 1)\delta_x]^2 + [(K_y - 2k_y + 1)\delta_y]^2} \quad (6)$$

$$\alpha_k = \text{atan2}\left((K_y - 2k_y + 1)\delta_y, (K_x - 2k_x + 1)\delta_x\right) \quad (7)$$

where $k_y = \left\lceil \frac{k}{K_x} \right\rceil$, $k_x = k - (k_y - 1)K_x$, and $\lceil \cdot \rceil$ denotes the ceiling function.

Proof: The travel distances $\varepsilon_{tk}(t)$ can be calculated as

$$\varepsilon_{tk}(t) = \sqrt{(x_{tk}(t))^2 + (y_{tk}(t))^2 + (z_{tk}(t))^2} \quad (8)$$

where

$$x_{tk}(t) = \varepsilon_t(t)\cos\theta_t\cos\phi_t + \Delta_k \cos\zeta_E(t)\cos(\zeta_A(t) + \alpha_k) \quad (9)$$

$$y_{tk}(t) = \varepsilon_t(t)\cos\theta_t\sin\phi_t + \Delta_k \cos\zeta_E(t)\sin(\zeta_A(t) + \alpha_k) \quad (10)$$

$$z_{tk}(t) = \varepsilon_t(t)\sin\theta_t + \Delta_k \sin\zeta_E(t). \quad (11)$$

By substituting (9)–(11) into (8), we have

$$\varepsilon_{tk}(t) = \{\varepsilon_t^2(t) + 2\varepsilon_t(t)\Delta_k[\cos\theta_t\cos\zeta_E(t) \times \cos(\alpha_k - \phi_t + \zeta_A(t)) + \sin\theta_t \sin\zeta_E(t)] + (\Delta_k \cos\zeta_E(t)(\zeta_A(t) + \alpha_k))^2 + (\Delta_k \cos\zeta_E(t) \times \sin(\zeta_A(t) + \alpha_k))^2 + (\Delta_k \sin\zeta_E(t))^2\}^{1/2}. \quad (12)$$

Under the far-field condition, i.e., $\Delta_k \ll \varepsilon_t(t)$ and using the approximation $\sqrt{1-x} \approx 1 - \frac{x}{2}$ when x is small, (12) is approximated as

$$\varepsilon_{tk}(t) \approx \varepsilon_t(t) + \Delta_k \cos\theta_t \cos\zeta_E(t)[\cos(\alpha_k - \phi_t)\cos\zeta_A(t) - \sin(\alpha_k - \phi_t)\sin\zeta_A(t)] + \Delta_k \sin\theta_t \sin\zeta_E(t). \quad (13)$$

Noting that $\max\{\zeta_E(t), \zeta_A(t)\} \ll 1$ rad, using the approximation $\sin(\zeta_{E(A)}(t)) \approx \zeta_{E(A)}(t)$, and $\cos(\zeta_{E(A)}(t)) \approx 1$, we can obtain (5). ■

Authorized licensed use limited to: Southeast University. Downloaded on July 12,2024 at 02:10:16 UTC from IEEE Xplore. Restrictions apply.

Proposition 2: The travel distances of RU_k–Rx at time t can be calculated as

$$\varepsilon_{kr}(t) \approx \varepsilon_r(t) + \Delta_k \cdot \cos\vartheta_r \cdot [\cos(\alpha_k - \varphi_r) - \sin(\alpha_k - \varphi_r) \cdot \zeta_A(t)] + \Delta_k \cdot \sin\vartheta_r \cdot \zeta_E(t) \quad (14)$$

where the time-varying distance from RIS center to the Rx is $\varepsilon_r(t) \approx \varepsilon_r + v_u t \cos\vartheta_r \cos(\varphi_r - \alpha_u) - v_r t \cos\vartheta_r \cos(\varphi_r - \alpha_r)$. The proof follows a similar procedure to the proof of Proposition 1 and is omitted due to limited space.

By substituting (5) and (14) into (4), after several mathematical manipulations, the CIR is given as

$$h_{\text{RIS}}(t,\tau) = \sum_{k=1}^{K} J_k e^{j\psi_k(t)} e^{j\frac{2\pi}{\lambda}(\varepsilon_t+\varepsilon_r)} e^{j2\pi(\nu_{tu}t+\nu_{ru}t-\nu_t t-\nu_r t)} \times e^{j\frac{2\pi}{\lambda}\Delta_k[\cos\theta_t\cos(\alpha_k-\phi_t)+\cos\vartheta_r\cos(\alpha_k-\varphi_r)]} \times e^{j\frac{2\pi}{\lambda}[P_k\zeta_A(t)+Q_k\zeta_E(t)]} \cdot \delta(\tau-\tau_k) \quad (15)$$

where $P_k = -\Delta_k[\cos\theta_t \sin(\alpha_k - \phi_t) + \cos\vartheta_r \sin(\alpha_k - \varphi_r)]$, $Q_k = \Delta_k(\sin\theta_t + \sin\vartheta_r)$. In addition, $\nu_t = \frac{v_t}{\lambda}\cos\theta_t\cos(\phi_t - \alpha_t)$ and $\nu_r = \frac{v_r}{\lambda}\cos\vartheta_r\cos(\varphi_r - \alpha_r)$ are Doppler shifts resulting from the movements of Tx and Rx, respectively. Moreover, $\nu_{tu} = \frac{v_u}{\lambda}\cos\theta_t\cos(\phi_t - \alpha_u)$ is Doppler shift stemming from the moving UAV affecting the wave emitted from the Tx, $\nu_{ru} = \frac{v_u}{\lambda}\cos\vartheta_r\cos(\varphi_r - \alpha_u)$ is Doppler shift caused by the moving UAV affecting the waves impinging on the Rx. It is clearly observed that the phases of h_{RIS} stemming from five components as follows

- $\psi_k(t)$ is the phase shift induced from RU_k.
- $\frac{2\pi}{\lambda}(\varepsilon_t+\varepsilon_r)$ is the phase shift caused by the travel distance at initial time instant.
- $\frac{2\pi}{\lambda}\Delta_k[\cos\theta_t\cos(\alpha_k-\phi_t)+\cos\vartheta_r\cos(\alpha_k-\varphi_r)]$ is the phase shift caused by the relative locations of different RUs.
- $2\pi(\nu_{tu}t+\nu_{ru}t-\nu_t t-\nu_r t)$ is the phase shift resulting from large-scale mobilities of UAV and ground nodes.
- $\frac{2\pi}{\lambda}[P_k\zeta_A(t)+Q_k\zeta_E(t)]$ is the phase shift caused by the micro-scale mobilities of UAV, i.e., UAV fluctuations. By defining $\tilde{\theta}(t) = \frac{2\pi}{\lambda}[P_k\zeta_A(t)+Q_k\zeta_E(t)]$, the UAV fluctuations introduce effective Doppler shifts, i.e.,

$$\frac{1}{2\pi}\frac{\mathrm{d}\tilde{\theta}(t)}{\mathrm{d}t} = \frac{2\pi}{\lambda} f_w \cdot (\xi_A P_k + \xi_E Q_k) \cdot \cos(2\pi f_w t). \quad (16)$$

For the Tx-Rx subchannel, the CIR is depicted by the widely used twin-cluster model as follows [12]

$$h_{\text{env}}(t,\tau) = \lim_{S_1,S_2\to\infty} \sum_{s_1=1}^{S_1}\sum_{s_2=1}^{S_2} J_{s_1s_2} \cdot e^{j\theta_{s_1s_2}} \times e^{j\frac{2\pi}{\lambda}[\varepsilon_{s_1s_2}-v_t t\cos\theta_{s_1}\cos(\phi_{s_1}-\alpha_t)]} \times e^{-j\frac{2\pi}{\lambda}v_r t\cos\vartheta_{s_2}\cos(\varphi_{s_2}-\alpha_r)} \cdot \delta(\tau-\tau_{s_1s_2}) \quad (17)$$

where $J_{s_1s_2} = \frac{1}{\sqrt{S_1S_2}}$, S_1 and S_2 are the number of the first and last bounces of scatterers, respectively, $\theta_{s_1s_2} \sim U[0, 2\pi)$, $\tau_{s_1s_2}$ and $\varepsilon_{s_1s_2}$ are the delay and travel distance of the ray via the s_1th and s_2th scatterers, $\tau_{s_1s_2} = \varepsilon_{s_1s_2}/c$. Furthermore, θ_{s_1} and ϕ_{s_1} are elevation and azimuth angles of departure of the ray impinging on the s_1th scatterer, respectively, ϑ_{s_2} and φ_{s_2} are elevation and azimuth angles of arrival of the ray via the s_2th scatterer, respectively. The typical values of the model parameters can be found in [12] and [13], which have been validated by several measurements.

C. Large-Scale Fading

The pathloss of the channel via the RIS is obtained as [14]

$$PL_{\text{RIS}}^{-1} = \frac{\delta_x\delta_y\lambda^2}{64\pi^3}\left|\sum_{k=1}^{K}\frac{e^{\frac{-j\{2\pi[\varepsilon_{tk}(t)+\varepsilon_{kr}(t)]+\lambda\psi_k(t)\}}{\lambda}}}{\varepsilon_{tk}(t)\varepsilon_{kr}(t)}\right|^2. \quad (18)$$

We assume that the RIS controller has the knowledge of the trajectories of the UAV and ground nodes. Since the UAV fluctuations are random and difficult to predict, the RIS phases are optimized to maximize the received power according to (18) based on the mean positions of each RU, i.e., $\psi'_k(t) = -\frac{2\pi}{\lambda}(\varepsilon_{tk}(t)+\varepsilon_{kr}(t))|_{\zeta_A(t)=0,\zeta_E(t)=0}$. By substituting (5) and (14) into the aforementioned RIS phases, we can obtain

$$\psi'_k(t) = -\frac{2\pi}{\lambda}[\varepsilon_t(t) + \Delta_k\cos\theta_t\cos(\alpha_k-\phi_t) + \varepsilon_r(t) + \Delta_k\cos\vartheta_r\cos(\alpha_k-\varphi_r)]. \quad (19)$$

The final reflection phases are $\psi_k(t) = \text{mod}(\psi'_k(t), 2\pi)$. By substituting (5), (14), and (19) into (18), and under the far-field condition, we have

$$PL_{\text{RIS}}^{-1} \approx \frac{\delta_x\delta_y\lambda^2}{64\pi^3\varepsilon_t^2(t)\varepsilon_r^2(t)}\left|\sum_{k=1}^{K} e^{j\frac{2\pi}{\lambda}\left[P_k\zeta_A(t)+Q_k\zeta_E(t)\right]}\right|^2. \quad (20)$$

It is apparently that $\frac{2\pi}{\lambda}[P_k\zeta_A(t)+Q_k\zeta_E(t)]$ represents the misaligned phases resulting from the random fluctuations. By setting $\zeta_A(t) = 0$ and $\zeta_E(t) = 0$, (20) reduces to $PL_{\text{RIS}}^{-1} \approx \frac{\delta_x\delta_y\lambda^2K^2}{64\pi^3\varepsilon_t^2(t)\varepsilon_r^2(t)}$, and is in consistency with the result in [14]. Note that (18) is derived based on the free-space pathloss model. However, for the Tx-Rx subchannel, NLoS paths can propagate via physical objects. Therefore, we adopt the close-in (CI) model as follows [11]

$$PL_{\text{env}}^{[\text{dB}]} = 20\log_{10}(\frac{4\pi f_c}{c}) + 10n_{\text{PLE}}\log_{10}\varepsilon_{tr} \quad (21)$$

where n_{PLE} is the pathloss exponent. The pathloss is converted into a linear scale as $PL_{\text{env}} = 10^{\frac{PL_{\text{env}}^{[\text{dB}]}}{10}}$.

III. Temporal Correlation Function

The TCF of the model is defined as $\rho(\Delta t) = \text{E}\{H(t,f)\cdot H^*(t-\Delta t, f)\}$, where $(\cdot)^*$ means the complex conjugate operation, $\text{E}\{\cdot\}$ is the expectation operation, $H(t,f)$ is the channel transfer function, i.e., $H(t,f) = \int_{-\infty}^{\infty} h(t,\tau)e^{-j2\pi f\tau}\mathrm{d}\tau$, and Δt represents time difference. Based on (3), TCF can be calculated as

$$\rho(\Delta t) = PL_{\text{RIS}}^{-1}\cdot\rho_{\text{RIS}}(\Delta t) + PL_{\text{env}}^{-1}\cdot\rho_{\text{env}}(\Delta t) \quad (22)$$

where the TCF of Tx-RIS-Rx subchannel is calculated as

$$\rho_{\text{RIS}}(\Delta t) = \text{E}\{\sum_{k=1}^{K} J_k^2 e^{j(\psi_k(t)-\psi_k(t-\Delta t))}\cdot e^{j2\pi\Delta t(\nu_{tu}+\nu_{ru}-\nu_t-\nu_r)}$$

Authorized licensed use limited to: Southeast University. Downloaded on July 12,2024 at 02:10:16 UTC from IEEE Xplore. Restrictions apply.

$$\times e^{j\frac{2\pi}{\lambda}P_k(\zeta_A(t)-\zeta_A(t-\Delta t))} \cdot e^{j\frac{2\pi}{\lambda}Q_k(\zeta_E(t)-\zeta_E(t-\Delta t))}\Big\}. \tag{23}$$

Assuming that $\xi_A \sim U[-\zeta_{Am}, \zeta_{Am})$ and $\xi_E \sim U[-\zeta_{Em}, \zeta_{Em})$ are independent random variables, where ζ_{Am} and ζ_{Em} define the maximum wobbling angles in the azimuth and elevation planes, respectively. Using $\mathrm{E}\{e^{jtx}\} = \frac{\exp(jtu)-\exp(jtl)}{(u-l)jt}$, where $x \sim U[u, l]$, the TCF can be further expressed as

$$\begin{aligned}\rho_{\text{RIS}}(\Delta t) = J_k^2 \sum_{k=1}^{K} e^{j(\psi_k(t)-\psi_k(t-\Delta t))} e^{j2\pi\Delta t(\nu_{tu}+\nu_{ru}-\nu_t-\nu_r)} \\ \times \int_{-\infty}^{\infty} \operatorname{sinc}\left(\frac{2}{\lambda}\zeta_{Am} \cdot P_k \cdot T(t,\Delta t)\right) p(f_w)\mathrm{d}(f_w) \\ \times \int_{-\infty}^{\infty} \operatorname{sinc}\left(\frac{2}{\lambda}\zeta_{Em} \cdot Q_k \cdot T(t,\Delta t)\right) p(f_w)\mathrm{d}(f_w)\end{aligned} \tag{24}$$

where $T(t,\Delta t) = \sin(2\pi f_w t) - \sin(2\pi f_w(t-\Delta t))$, $\operatorname{sinc}(x) = \frac{\sin(\pi x)}{\pi x}$ is the sinc function, $p(f_w)$ is the probability density function (PDF) of f_w.

In the Tx-Rx subchannel, we use the von Mises PDFs to describe the azimuth angles at Tx and Rx sides, and are defined as [4]: $p(\phi_{s_1}) = \frac{e^{\kappa_t \cos(\phi_{s_1}-\mu_t)}}{2\pi I_0(\kappa_t)}$ and $p(\varphi_{s_2}) = \frac{e^{\kappa_r \cos(\varphi_{s_2}-\mu_r)}}{2\pi I_0(\kappa_r)}$, respectively, where $I_0(\cdot)$ is the zeroth-order modified Bessel function of the first kind. Besides, the cosine PDFs are used to characterize the elevation angles at the Tx and Rx sides, i.e., $p(\theta_{s_1}) = \frac{\pi}{4\theta_m}\cos(\frac{\pi}{2}\frac{\theta_{s_1}}{\theta_m})$ and $p(\vartheta_{s_2}) = \frac{\pi}{4\vartheta_m}\cos(\frac{\pi}{2}\frac{\vartheta_{s_2}}{\vartheta_m})$, respectively, where θ_m and ϑ_m are maximum elevation angles. The TCF of the Tx-Rx subchannel is calculated as

$$\begin{aligned}\rho_{\text{env}}(\Delta t) = \int_{-\vartheta_m}^{\vartheta_m}\int_{-\theta_m}^{\theta_m}\int_{-\pi}^{\pi}\int_{-\pi}^{\pi} e^{-j\frac{2\pi}{\lambda}\Delta t v_t \cos\theta_{s_1}\cos(\phi_{s_1}-\alpha_t)} \\ \times e^{-j\frac{2\pi}{\lambda}\Delta t v_r \cos\vartheta_{s_2}\cos(\varphi_{s_2}-\alpha_r)} \\ \times p(\phi_{s_1})p(\varphi_{s_2})p(\theta_{s_1})p(\vartheta_{s_2})\mathrm{d}\phi_{s_1}\mathrm{d}\varphi_{s_2}\mathrm{d}\theta_{s_1}\mathrm{d}\vartheta_{s_2}.\end{aligned} \tag{25}$$

Using the formula [15, eq. 3.338–4], (25) is calculated as

$$\begin{aligned}\rho_{\text{env}}(\Delta t) \\ = \int_{-\theta_m}^{\theta_m} \frac{\pi\cos(\frac{\pi\theta_{s_1}}{2\theta_m})}{4\theta_m I_0(\kappa_t)} \cdot I_0\big(\sqrt{A_t^2(\theta_{s_1}) + B_t^2(\theta_{s_1})}\big)\mathrm{d}\theta_{s_1} \\ \times \int_{-\vartheta_m}^{\vartheta_m} \frac{\pi\cos(\frac{\pi\vartheta_{s_2}}{2\vartheta_m})}{4\vartheta_m I_0(\kappa_r)} \cdot I_0\big(\sqrt{A_r^2(\vartheta_{s_2}) + B_r^2(\vartheta_{s_2})}\big)\mathrm{d}\vartheta_{s_2}\end{aligned} \tag{26}$$

where

$$A_t(\theta_{s_1}) = \kappa_t\cos\mu_t - j2\frac{\pi}{\lambda}\Delta t v_t\cos\theta_{s_1}\cos\alpha_t \tag{27}$$

$$B_t(\theta_{s_1}) = \kappa_t\sin\mu_t - j2\frac{\pi}{\lambda}\Delta t v_t\cos\theta_{s_1}\sin\alpha_t \tag{28}$$

$$A_r(\vartheta_{s_2}) = \kappa_r\cos\mu_r - j2\frac{\pi}{\lambda}\Delta t v_r\cos\vartheta_{s_2}\cos\alpha_r \tag{29}$$

$$B_r(\vartheta_{s_2}) = \kappa_r\sin\mu_r - j2\frac{\pi}{\lambda}\Delta t v_r\cos\vartheta_{s_2}\sin\alpha_r. \tag{30}$$

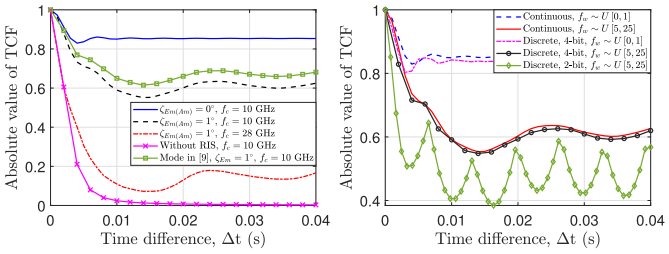

(a) (b)

Fig. 3. The impacts of UAV vibrations on TCFs with different (a) amplitudes and (b) frequencies of the vibration angles ($\zeta_{Am} = \zeta_{Em} = 1^\circ$ and $f_c = 10$ GHz).

Note that the integrand in (26) is an even function, and θ_{s_1} and ϑ_{s_2} are small angles, we use the Simpson's 1/3 rule [16] to solve the integrals in (26) as follows

$$\begin{aligned}\rho_{\text{env}}(\Delta t) \\ \approx \frac{\pi^2}{36 I_0(\kappa_t) I_0(\kappa_r)} \\ \times\left[\frac{1}{2}I_0\Big(\sqrt{A_t^2(0)+B_t^2(0)}\Big)+\sqrt{2}I_0\Big(\sqrt{A_t^2(\frac{\theta_m}{2})+B_t^2(\frac{\theta_m}{2})}\Big)\right] \\ \times\left[\frac{1}{2}I_0\Big(\sqrt{A_r^2(0)+B_r^2(0)}\Big)+\sqrt{2}I_0\Big(\sqrt{A_r^2(\frac{\vartheta_m}{2})+B_r^2(\frac{\vartheta_m}{2})}\Big)\right].\end{aligned} \tag{31}$$

IV. Results and Discussions

In the simulations, the default model parameters are selected as follows [4]: $\mu_t = 70^\circ$, $\mu_r = 20^\circ$, $\theta_m = \vartheta_m = 10^\circ$, $\kappa_t = \kappa_r = 20$, $\alpha_t = \alpha_r = \alpha_u = \pi/4$, $\delta_x = \delta_y = \frac{\lambda}{2}$, $K_x = K_y = 50$, $\varepsilon_{tr} = 200$ m, $f_w \sim U(5, 25)$ Hz [9]. The UAV is traveling at a speed of 19 m/s, while both the Tx and Rx are maintaining a speed of 18 m/s. In addition, the UAV is initially positioned at $(200, 90, 150)$ m. Fig. 3(a) illustrates the TCFs of the model with different amplitudes of vibration angles and carrier frequencies. By setting $\zeta_{Em(Am)} = 0^\circ$, the channel illustrates the highest TCF and behaves like a virtual LoS path. In this case, the phases of signals reflected by the RIS are accurately aligned by the tunable reflection phases, which effectively mitigates the multipath effects. However, when the UAV vibration is considered, the UAV location uncertainty results in phase misalignment of the signals, leading to a lower TCF. In addition, when the system operating at high frequencies, e.g., 28 GHz, the TCF decorrelates faster, indicating a shorter coherence time compared to those at 10 GHz. This indicates that the ARIS is more susceptible to the UAV vibrations for high frequency bands. Under the same degree of vibration, the TCF generated using the fluctuation model in [9] illustrates a relatively high value. This is attributed to the fact that in [9], only pitch angle fluctuation was considered. In addition, Fig. 3(b) investigates the impacts of vibration frequencies on channel TCF with different reflection phase configurations. As the vibration frequencies increase, the channel decorrelates faster. Under the same vibration conditions, the channels with continuous and 4-bit discrete reflection phases behave similarly in TCF. However, the TCF with 2-bit discrete reflection phases reduces significantly compared to the continuous one due to the increased quantization errors.

Authorized licensed use limited to: Southeast University. Downloaded on July 12,2024 at 02:10:16 UTC from IEEE Xplore. Restrictions apply.

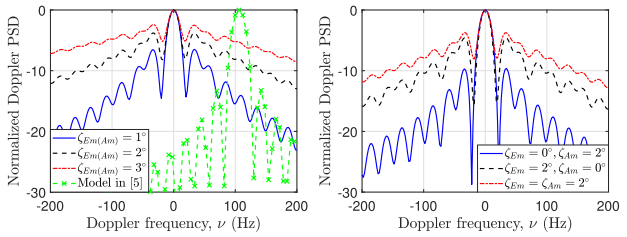

Fig. 4. The impacts of UAV fluctuations on Doppler PSDs with different yaw and/or pitch angles.

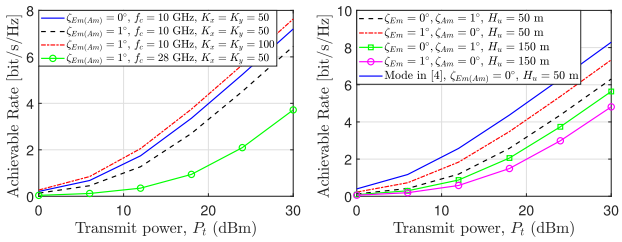

Fig. 5. The impacts of UAV fluctuations on the achievable rates of the ARIS system with (a) different carrier frequencies, RU numbers, and (b) UAV altitudes.

Fig. 4(a) shows the impacts of UAV fluctuations on Doppler PSDs at $f_c = 28$ GHz, which is obtained as $S(\nu) = \int_{-\infty}^{\infty} \rho(\Delta t) e^{-j2\pi\nu\Delta t} \mathrm{d}(\Delta t)$. The UAV fluctuations introduce extra Doppler frequency components and broaden the Doppler PSD range. Larger vibration angles imply the UAV fluctuates severely, which results in larger Doppler spreads. Although the optimized reflection phases presented in [5] effectively mitigate multipath fading, they are unable to offset the rapid phase variations induced by Doppler frequencies. Fig. 4(b) reveals that the pitch angle has a more pronounced effect on Doppler PSDs compared to the yaw angle when $H_u = 150$ m. The Doppler PSD illustrates a widest range when the UAV experiences vibrations simultaneously in horizontal and vertical directions.

Fig. 5 shows the ergodic achievable rate of the ARIS system, which is obtained as $C = \mathrm{E}\{\log_2(1+\rho)\}$, where $\rho = \frac{|h(t)|^2 P_t}{P_N}$ is the received instantaneous signal-to-noise ratio, P_t and P_N are transmit and noise powers, respectively, where $P_N = -100$ dBm [17]. As is shown in Fig. 5(a), the UAV fluctuation degrades the achievable rate performance due to the phase imperfection. A more noticeable degradation is observed when the carrier frequency increases. Note that the degradation in achievable rate can be compensated by adopting a larger RIS. An interesting observation is presented in Fig. 5(b). When the UAV hovers at a low altitude (relative to the horizontal distance of Tx-Rx), the yaw angle plays a more significant role in reducing the achievable data rate compared to the pitch angle. Conversely, when the UAV operates at a relatively high altitude, the pitch angle becomes more influential. The models, e.g., [4], which do not consider the UAV fluctuations and neglect the severe product-distance pathloss, may overestimate the system achievable rate.

V. Conclusion

In this letter, we have proposed a 3D ARIS channel model considering large-scale and small-scale fading with random UAV vibrations. We have shown that the UAV vibrations can decrease the temporal correlation of the RIS-assisted channel and introduce extra Doppler frequencies, and hence enlarge Doppler spread. Besides, the UAV vibrations lead to a degradation in achievable rates of ARIS systems. We have shown that the effects of yaw angle and pitch angle on the achievable rates vary when the UAV flies at different altitudes. Even for small UAV fluctuations, ARIS channel characteristics can be greatly impacted, especially for the system at high frequency bands. For future research, more advanced methods for optimizing RIS phase shifts will be investigated through the development of UAV vibration forecasting techniques.

References

[1] A. S. Abdalla, T. F. Rahman, and V. Marojevic, "UAVs with reconfigurable intelligent surfaces: Applications, challenges, and opportunities," 2020, *arXiv:2012.04775*.

[2] O. Darwish, A. Al-Fuqaha, M. Anan, and N. Nasser, "The role of hierarchical entropy analysis in the detection and time-scale determination of covert timing channels," in *Proc. Int. Wireless Commun. Mobile Comput. Conf. (IWCMC)*, Dubrovnik, Croatia, Aug. 2015, pp. 153–159.

[3] J. Walatkiewicz and O. Darwish, "A survey on drone cybersecurity and the application of machine learning on threat emergence," in *Proc. ACR*, Orlando, FL, USA, May 2023, pp. 523–532.

[4] H. Jiang, R. He, C. Ruan, J. Zhou, and D. Chang, "Three-dimensional geometry-based stochastic channel modeling for intelligent reflecting surface-assisted UAV MIMO communications," *IEEE Wireless Commun. Lett.*, vol. 10, no. 12, pp. 2727–2731, Sep. 2021.

[5] B. Xiong, Z. Zhang, H. Jiang, J. Zhang, L. Wu, and J. Dang, "A 3D non-stationary MIMO channel model for reconfigurable intelligent surface auxiliary UAV-to-ground mmWave communications," *IEEE Trans. Wireless Commun.*, vol. 21, no. 7, pp. 5658–5672, Jul. 2022.

[6] Y. Li, C. Yin, T. Do-Duy, A. Masaracchia, and T. Q. Duong, "Aerial reconfigurable intelligent surface-enabled URLLC UAV systems," *IEEE Access*, vol. 9, pp. 140248–140257, 2021.

[7] H. Lu, Y. Zeng, S. Jin, and R. Zhang, "Aerial intelligent reflecting surface: Joint placement and passive beamforming design with 3D beam flattening," *IEEE Trans. Wireless Commun.*, vol. 20, no. 7, pp. 4128–4143, Jul. 2021.

[8] Z. Ma et al., "Multipath fading channel modeling with aerial intelligent reflecting surface," in *Proc. IEEE Global Commun. Conf. (GLOBECOM)*, Madrid, Spain, Dec. 2021, pp. 1–6.

[9] M. Banagar, H. S. Dhillon, and A. F. Molisch, "Impact of UAV wobbling on the air-to-ground wireless channel," *IEEE Trans. Veh. Technol.*, vol. 69, no. 11, pp. 14025–14030, Nov. 2020.

[10] S. Yang, Z. Zhang, J. Zhang, and J. Zhang, "Impact of rotary-wing UAV wobbling on millimeter-wave air-to-ground wireless channel," *IEEE Trans. Veh. Technol.*, vol. 71, no. 9, pp. 9174–9185, Sep. 2022.

[11] T. S. Rappaport, Y. Xing, G. R. MacCartney, A. F. Molisch, E. Mellios, and J. Zhang, "Overview of millimeter wave communications for fifth-generation (5G) wireless networks-with a focus on propagation models," *IEEE Trans. Antennas Propag.*, vol. 65, no. 12, pp. 6213–6230, Dec. 2017.

[12] J. Bian, C.-X. Wang, X. Gao, X. You, and M. Zhang, "A general 3D non-stationary wireless channel model for 5G and beyond," *IEEE Trans. Wireless Commun.*, vol. 20, no. 5, pp. 3211–3224, May 2021.

[13] C.-X. Wang et al., "Pervasive wireless channel modeling theory and applications to 6G GBSMs for all frequency bands and all scenarios," *IEEE Trans. Veh. Technol.*, vol. 71, no. 9, pp. 9159–9173, Sep. 2022.

[14] W. Tang et al., "Wireless communications with reconfigurable intelligent surface: Path loss modeling and experimental measurement," *IEEE Trans. Wireless Commun.*, vol. 20, no. 1, pp. 421–439, Jan. 2021.

[15] I. S. Gradshteyn and I. M. Ryzhik, *Table of Integrals, Series, and Products*. New York, NY, USA: Academic, 2014.

[16] A. Horwitz, "A version of Simpson's rule for multiple integrals," *J. Comput. Appl. Math.*, vol. 134, nos. 1–2, pp. 1–11, Sep. 2001.

[17] E. Basar and I. Yildirim, "Reconfigurable intelligent surfaces for future wireless networks: A channel modeling perspective," *IEEE Wireless Commun.*, vol. 28, no. 3, pp. 108–114, Jun. 2021.

Authorized licensed use limited to: Southeast University. Downloaded on July 12,2024 at 02:10:16 UTC from IEEE Xplore. Restrictions apply.